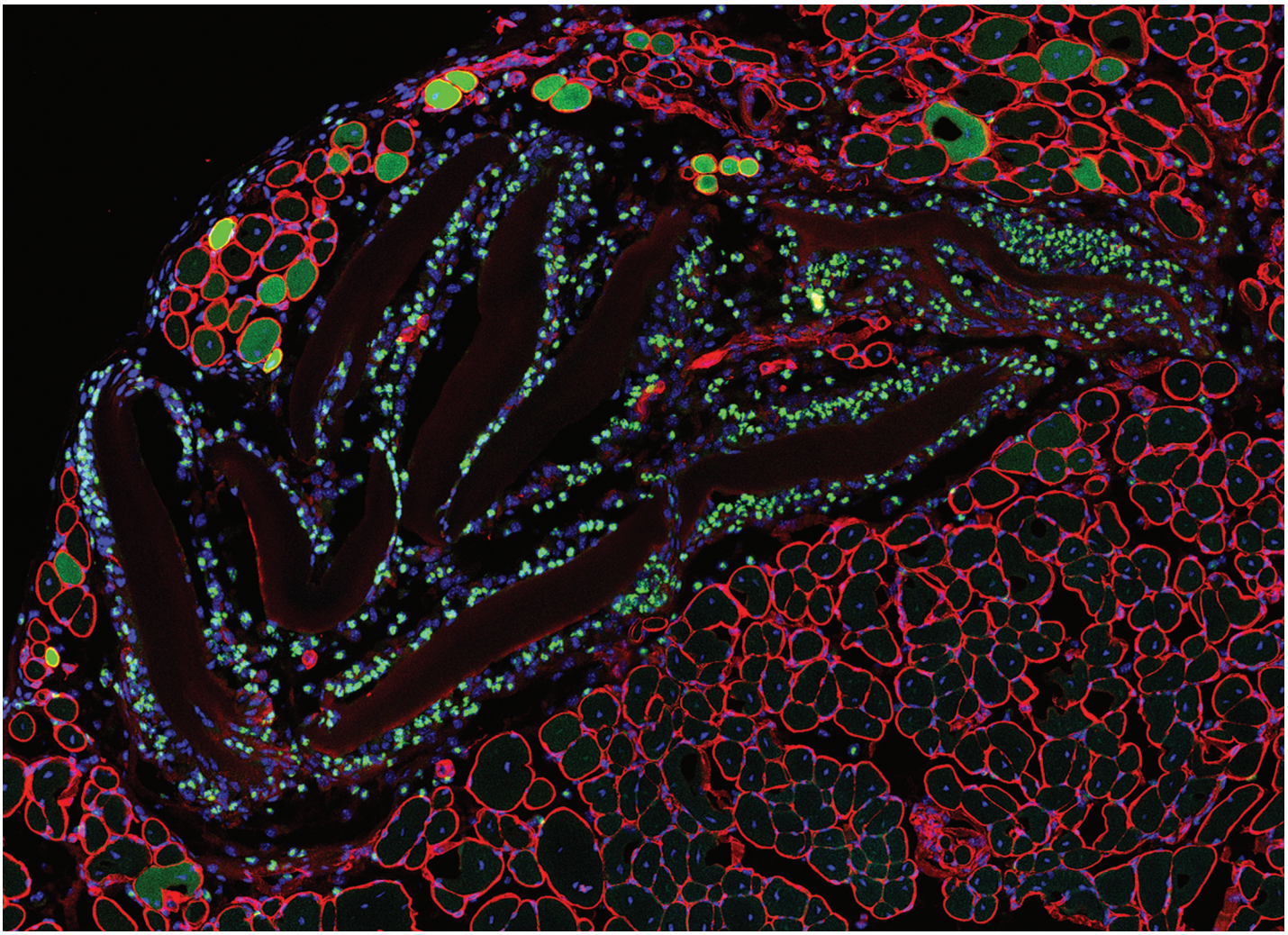

Showcasing research from Krista M. Habing's laboratory, Department of Biomedical Engineering, Oregon Health & Science University

Age-associated functional healing of musculoskeletal trauma through regenerative engineering and rehabilitation

Immunofluorescent staining of mouse skeletal muscle that has been treated with engineered muscle consisting of GFP+ myogenic cells on nanofibrillar scaffolds in combination with running exercise following volumetric muscle injury.

As featured in:

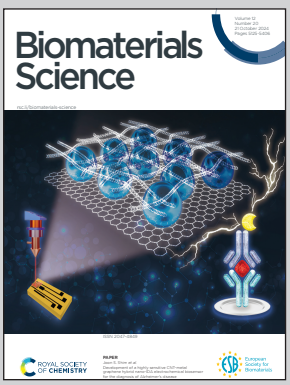

See Krista M. Habing *et al.*, *Biomater. Sci.*, 2024, **12**, 5186.

ROYAL SOCIETY OF CHEMISTRY

rsc.li/biomaterials-science

Registered charity number: 207890

Biomaterials Science

ROYAL SOCIETY OF CHEMISTRY

PAPER

View Article Online
View Journal | View Issue

Cite this: *Biomater. Sci.*, 2024, **12**, 5186

Age-associated functional healing of musculoskeletal trauma through regenerative engineering and rehabilitation†

Krista M. Habing, [a] Cynthia A. Alcazar, [a] Victoria R. Duke, [a] Yong How Tan, [a] Nick J. Willett[a,b,c,d] and Karina H. Nakayama *[a,c]

Traumatic musculoskeletal injuries that lead to volumetric muscle loss (VML) are challenged by irreparable soft tissue damage, impaired regenerative ability, and reduced muscle function. Regenerative rehabilitation strategies involving the pairing of engineered therapeutics with exercise have guided considerable advances in the functional repair of skeletal muscle following VML. However, few studies evaluate the efficacy of regenerative rehabilitation across the lifespan. In the current study, young and aged mice are treated with an engineered muscle, consisting of nanofibrillar-aligned collagen laden with myogenic cells, in combination with voluntary running activity following a VML injury. Overall, young mice perform at higher running volumes and intensities compared to aged mice but exhibit similar volumes relative to age-matched baselines. Additionally, young mice are highly responsive to the dual treatment showing enhanced force production ($p < 0.001$), muscle mass ($p < 0.05$), and vascular density ($p < 0.01$) compared to age-matched controls. Aged mice display upregulation of circulating inflammatory cytokines and show no significant regenerative response to treatment, suggesting a diminished efficacy of regenerative rehabilitation in aged populations. These findings highlight the restorative potential of regenerative engineering and rehabilitation for the treatment of traumatic musculoskeletal injuries in young populations and the complimentary need for age-specific interventions and studies to serve broader patient demographics.

Received 4th May 2024,
Accepted 12th August 2024

DOI: 10.1039/d4bm00616j

rsc.li/biomaterials-science

Introduction

The achievement of full functional restoration and healing in severely compromised musculoskeletal tissues represents an enduring clinical challenge. Despite endogenous self-repair mechanisms, severe volumetric muscle loss (VML) injuries (>20% muscle mass)[1] can lead to tissue fibrosis and a permanent loss of muscle structure and function. Current surgical management of VML involves the transfer of free or adjacent muscle flaps. While these strategies are limb-saving, they often fail to fully restore function,[2–4] leaving approximately half of patients with chronic pain and disability.[5]

Regenerative therapies that target both structural and functional repair of damaged skeletal muscle are primed for shifting the clinical management of VML injuries towards engineered alternatives. Preclinical evaluation of tissue engineering strategies has shown significant progress, including prevention of muscle atrophy, restoration of muscle mass, enhanced histological and genetic markers of myogenesis, and improved muscle force production in some cases.[6–10] Previously, we have shown that engineered muscle (EM) fabricated from aligned nanofibrillar collagen materials laden with myogenic cells or growth factors promoted vascular perfusion and myogenesis in a murine model of VML.[11–13] The regenerative capacity of these engineered therapies was further enhanced when combined with exercise rehabilitation by supporting increased neuro-vascularization. The landscape of regenerative therapies is likely to evolve in parallel with integration of physical rehabilitation.

Physical therapy is routinely prescribed to patients recovering from musculoskeletal trauma to increase mobility and preserve strength. The physiological response to physical activity supports increased blood flow, stem cell activation, growth factor production, modulation of the immune response, and facilitation of extracellular matrix remodeling.[14–18] However, there is no uniform clinical consensus for physical therapy regimens following VML as cases are highly heterogenous and even under ideal conditions, patients still face functional deficits and disability.[19,20] This highlights an unmet clinical need

[a]*Department of Biomedical Engineering, Oregon Health & Science University, Portland, OR, USA. E-mail: nakayaka@ohsu.edu; Tel: +1 503-418-9307*
[b]*Knight Campus for Accelerating Scientific Impact, University of Oregon, Eugene, OR, USA*
[c]*Department of Orthopaedics, Oregon Health & Science University, Portland, OR, USA*
[d]*The Veterans Affairs Portland Health Care System, Portland, OR, USA*
† Electronic supplementary information (ESI) available. See DOI: https://doi.org/10.1039/d4bm00616j

for therapies that can synergize with physical activity and mechanical stimuli to drive regenerative rehabilitation.[21] Previously developed engineered therapeutics demonstrated enhanced myogenesis, vascularization, and innervation through pairing with voluntary wheel running in a mouse VML injury.[11,13] Furthermore, studies have demonstrated that regenerative rehabilitation strategies also improve muscle force production following VML.[22] Although physical therapy alone has not yet been shown to fully restore VML-related functional deficits, optimized regimens, which can be influenced by factors such as timing and intensity, can facilitate synergistic healing responses and improve the regenerative effects of tissue engineered therapeutics. However, if not properly optimized, these regimens could have minimal impact or even potentially hinder regeneration. Therefore, with evidence-based rational design, regenerative rehabilitation strategies hold promise for enhancing recovery outcomes in VML patients.

An underserved population in VML and rehabilitation research is the aged demographic. The population of interest for the development of VML treatment strategies has historically been active military service members (median age 25–34),[23] leading to a large majority of preclinical VML repair studies being performed with young animals (age less than half the median lifespan of the animal).[11–13,22] However, severe musculoskeletal trauma is not limited to a military context and frequently affects civilian populations across the age spectrum. The prevalence of musculoskeletal trauma among civilians over fifty years of age varies from 10–50% depending upon the underlying cause of injury.[24–26] Skeletal muscle undergoes a deep spread of pathological changes with advancing age including fewer functional satellite cells, mitochondrial dysfunction, chronic inflammation, and increased insulin resistance,[27–29] all of which could impair muscle regeneration and the response to regenerative therapy following VML.

Studies investigating VML recovery in the context of aging are rare, and of the few that have explored tissue engineered therapeutics, aging has been shown to hinder regeneration.[30–32] Therefore, to assess the therapeutic efficacy of a regenerative rehabilitation strategy across an age-diverse population, the current study evaluates an EM therapy in combination with running exercise following a VML injury in both young and aged mice. Findings from this study will determine (1) the therapeutic potential of engineered skeletal muscle and exercise rehabilitation; (2) if combinatorial therapies support additive healing; (3) age-related limitations and differential healing responses to regenerative therapies. These studies establish several foundational cornerstones for the future development of age-specific engineered therapies for the treatment of musculoskeletal trauma.

Materials and methods

Experimental design

The objective of this study was to evaluate a regenerative rehabilitation therapy consisting of engineered muscle (EM) in combination with voluntary wheel running for treatment of a VML injury in both young and aged mice. The engineered muscle consisted of GFP+ primary mouse myogenic cells differentiated on collagen type I substrates composed of aligned nanofibrils. A total of 6 groups were evaluated that differed in age, exercise, and treatment with engineered muscle as follows: (1) young (Y), (2) young + exercise (Y_{Ex}), (3) young + exercise + engineered muscle (Y_{Ex+EM}), (4) aged (A), (5) aged + exercise (A_{Ex}), (6) aged + exercise + engineered muscle (A_{Ex+EM}). The efficacy of the applied therapies was assessed using running metrics, muscle physiology, tissue morphometrics, immunofluorescent markers for myogenesis and neurovascularization, and cytokine profiling.

Isolation and culture of GFP + primary mouse myoblasts

Primary myoblast isolation and culture was adapted from Shahini *et al.*[33] Briefly, major skeletal muscle groups were harvested from 5-week-old male C57BL/6-Tg(CAG-EGFP)131Osb/LeySopJ mice obtained from Jackson Laboratories. Muscle was minced and then digested for 30 minutes at 37 °C in a solution of enzymes containing 500 U mL^{-1} collagenase type II (Worthington), 1.5 U mL^{-1} collagenase D (Sigma Aldrich), 2.5 U mL^{-1} dispase II (Gibco), and 2.5 mM calcium chloride. Digested tissues were seeded at 20–30% surface coverage into 0.9 mg mL^{-1} Matrigel-coated (Corning) tissue culture flasks containing growth media. Growth media consisted of Dulbecco's Modified Eagle Medium (DMEM, Gibco), 20% fetal bovine serum (Gibco), 10% horse serum (Gibco), 1% antibiotic-antimycotic (Gibco), 0.5% chicken embryo extract (United States Biological Corporation), 2.5 ng mL^{-1} basic fibroblast growth factor (PeproTech), 10 μg mL^{-1} gentamycin (Gibco), and 2.5 μg mL^{-1} plasmocin prophylactic (Invivogen). Myoblasts grew out from the tissues until 80% confluency was reached. For the first two passages, myoblasts were pre-plated by incubation at 37 °C for one hour on 0.1 mg mL^{-1} rat-tail collagen I (Corning) coated flasks to remove non-myogenic cells before transferring the remaining suspended cells to 0.09 mg mL^{-1} Matrigel (Corning) coated flasks at 5000 cells per cm^2.

The purity of the myoblast population was assessed using immunocytochemical analysis following the first pre-plate. Cells were fixed in 4% paraformaldehyde (PFA) for 10 minutes, followed by permeabilization in 0.1% Triton-X 100 for 15 minutes, and blocking in 5% goat serum for 1 hour. The culture was incubated with mouse anti-MyoD, an early myogenic marker, (1 : 100, overnight, 4 °C, BD Biosciences) which was then conjugated to goat anti-mouse Alexa Fluor 647 (1 : 200, 1 hour, room temperature, Invitrogen). Cells were mounted with VectaShield with DAPI (Vector Laboratories). Tiled and *z*-stacked images were collected using the Zeiss LSM 900 confocal microscope at 20× magnification. Cells of a myogenic lineage were quantified by their consistent nuclear expression of MyoD and normalized to the number of total nuclei ($N = 5$).

Fabrication of engineered muscle constructs

EM constructs were fabricated as described in previous publications.[11–13] Briefly, high-density collagen (30 mg mL^{-1})

was obtained by dialyzing rat-tail collagen type I (10 mg mL^{-1}, Corning) in Seamless Cellulose Dialysis Tubing (Fisher Scientific) on a bed of polyethylene glycol for 35 minutes at 4 °C. Aligned fibrillogenesis was initialized by extruding chilled high-density collagen from a blunt 22 G needle at an approximately 30° angle and a velocity of 340 mm s^{-1} into warmed 10X phosphate buffered saline (PBS, pH 7.4, 37 °C). Eight extruded scaffolds (1 mm diameters) were assembled in parallel on pre-cut Nexterion hydrophobic glass chips (Schott) to create the collagen base of the transplantable construct (1 mm × 8 mm × 22 mm). The scaffolds were partially dried for 2 hours, washed in 1× PBS, and allowed to dry again overnight. The collagen scaffolds were prepared for cell culture by 70% ethanol sterilization and successive PBS washes. GFP+ primary myoblasts were seeded at approximately 400 000 cells per scaffold and cultured for 2 days in growth medium. EM constructs were switched to differentiation medium containing DMEM (Gibco), 5% horse serum (Gibco), and 1% antibiotic-antimycotic (Gibco) for an additional 6–7 days to allow for myotube fusion prior to transplantation.

Scanning electron microscopy of collagen scaffolds

To prepare the collagen scaffolds for scanning electron microscopy (SEM), the collagen scaffolds were mounted on conductive Indium Tin Oxide (ITO, SPI Supplies) coverslips. The collagen scaffolds were dried overnight prior to consecutive fixation in 2.5% glutaraldehyde in 0.5 M sodium cacodylate buffer (Electron Microscopy Sciences) and 2% aqueous osmium tetroxide (Ted Pella), with washing in between using deionized water. Post fixation, the collagen scaffolds were dehydrated in an ethanol series (30%, 50%, 75%, 85%, 95%, 100%, 100%) before further dehydration in a Leica CPD300 critical point dryer (Leica Microsystems, Germany). The dehydrated collagen scaffolds on the ITO coverslips were then mounted on aluminum pins with carbon tabs and coated with 8 nm of carbon in a Leica ACE600 sputter coater (Leica Microsystems, Germany). To ensure full conductivity around the edges of the scaffolds, additional silver paint was added around the ITO coverslips. To image the scaffolds, a FEI Helios G3 NanoLab DualBeam electron microscope was used with beam conditions of 2 keV, 25–100 pA, and 4–5 mm working distance. The images were captured at 50 000× magnification and saved using a 6144 × 4096 image size and 1 μs pixel dwell time. ImageJ's jPOR[34] and FibrilTool[35] plugins were used to quantify collagen scaffold porosity and anisotropy, respectively ($N = 3$).

Immunocytochemical characterization of the engineered construct

EM was fixed in 4% PFA, followed by permeabilization in 0.1% Triton-X 100 for 15 minutes, and blocking in 1% bovine serum albumin (BSA) for 30 minutes. EM was incubated with rabbit anti-fast skeletal myosin heavy chain (1 : 500, overnight, 4 °C, Abcam), goat anti-rabbit Alexa Fluor 555 (1 : 200, 1 hour, room temperature, Invitrogen), and Hoechst (1 : 500, 15 minutes, room temperature, BD Biosciences). 9 × 3 tiled *z*-stacked images were collected using the Zeiss LSM 900 confocal microscope at 20× magnification and then quantified using MyoCount 1.3 ($N = 4$) to obtain percent myotube coverage and Fusion Index.[36] The following parameters were used for analysis: SmallestMyotubePixelCount = 200, SmallestNucleusPixelCount = 50, NucFillSize = 2, MaxCircleRad = 30, MaxNucSizeDivisor = 200, and TubeThresh = 1.07. Using MyoCount, Fusion Index (% nuclei within MHC + myotubes, with at least 3 nuclei) and myotube formation (% image area covered by myotubes) were obtained.

Transplantation of engineered muscle into a mouse volumetric muscle loss injury model

All animal procedures were performed in accordance with the Guidelines for Care and Use of Laboratory Animals of the Oregon Health & Science University (OHSU) and approved by the OHSU Institutional Animal Care and Use Committee (Protocol number: TR01_IP00002839).

C57BL/6J male mice were obtained from Jackson Laboratories and used at 8 weeks or 80 weeks of age which roughly parallels human ages of 18 and 60 years.[37] Mice were anesthetized using 3% isoflurane with 100% oxygen flow rate of 1 L min^{-1} and administered pre-surgical subcutaneous analgesic (Buprenorphine Extended Release, 1 mg kg^{-1}), antibiotic (Baytril, 5 mg kg^{-1}), and sterile saline (0.9% sodium chloride, 5% w/v). Hair was removed from the hindlimbs with depilation cream, and the surgical area was aseptically prepared with iodine and alcohol. Surgical volumetric muscle loss (VML) was induced as previously described.[11–13] In short, a 20–30% muscle defect was created in the tibialis anterior (TA) muscle ($N \geq 8$ each age) by surgical ablation measuring approximately 7 mm × 2 mm × 2 mm at the TA midline. Percent ablation was verified by comparing the mass of the surgically excised tissue to the post-mortem mass of the uninjured control TA muscle in a subset of mice. Mice which received an EM construct had the construct implanted and secured with 10–0 non-absorbable nylon suture loops at the distal and proximal ends of the defect. The medial and lateral edges of the defect were closed over the EM and secured by a cruciate knot with 8–0 non-absorbable nylon followed by skin closure with a continuous suture of the same material.

Plasma collection and Luminex analysis

Plasma samples were collected longitudinally at baseline and at 1-, 2-, and 4-weeks post-surgery. Mice were anesthetized with 3% isoflurane and a heparinized capillary tube (Fisher Scientific) was inserted into the medial canthus of the eye. 100 μL of blood was collected each session and blood was alternately drawn from the left and right eyes. The blood was then centrifuged at 2000*g* for 20 minutes to facilitate separation of the blood components. The plasma fraction was collected and stored at −80 °C until Luminex analysis was performed.

Plasma was analyzed for cytokines using the Milliplex MAP Mouse Cytokine/Chemokine Magnetic Bead Panel (Millipore Sigma). The panel was read using a Luminex 200 (Luminex)

and the median fluorescent intensity values (MFI) and bead counts were recorded. A subset of samples was run to determine the sample dilution needed to be within the linear range of detection of the Luminex 200. MFI data was analyzed using RStudio. Cytokines with average bead counts <25 and average MFI values <15 were excluded from analysis as they were below the limit of detection for this system. The remaining cytokines used in analysis were: G-CSF, Eotaxin, IFNγ, IL-4, IL-3, IL-5, IL-6, IL-7, IL-10, IL-12(p40), LIF, IL-13, LIX, IL-15, IL-17, IP-10, KC, MIP-1β, MIG, VEGF, and TNFα. Briefly, the data was log-transformed ($\log_{10}(x + 1)$), corrected for batch effect using the removeBatchEffect( ) function in the LIMMA R package, outliers were removed using interquartile range, and then the remaining values were *z*-score normalized.

Free running exercise program

A subset of mice underwent a voluntary free running exercise program utilizing single housing cages containing activity wheels (Scurry Mouse Running Wheel 80820S, Lafayette Instrument). Running activity was recorded every 3 seconds and binned every 15 seconds using digital counters (Scurry Mouse Activity Counter 86110, Lafayette Instrument) and Scurry Software v20.08.19 (Lafayette Instrument). Mice were acclimated to the activity wheels for 72 hours prior to surgery to establish baseline running distances. Mice displaying both relatively high and low baseline distances were equitably distributed among the surgical groups (±EM) to ensure a balanced inclusion of mice with varied running capabilities across each group ($N \geq 8$ each group). After the surgery, mice underwent a 7-day recovery period in conventional group housing. This recovery period was chosen as it has been demonstrated that earlier introduction of exercise delayed muscle regeneration and increased fibrosis.[22] Following the 7-day recovery period, mice designated for exercise were returned to their original activity wheel housing for 21 days, while the remaining mice continued with conventional group housing and normal cage activity.

The timeline of daily running distances was created by comparing the final 24 hours of baseline running distance with the initial and final 24-hour periods of running distances post-surgery. Other running metrics (durations, bouts, velocities) were averaged over the 21-day exercise program and compared between ages rather than experimental groups. Metrics were quantified using a custom C++ code.

In situ muscle force production

The maximum isometric force produced by the TA muscle was evaluated at 28 days post-surgery. Mice were anesthetized with 1–3% isoflurane and hindlimb fur was removed. The TA muscle was exposed by removing the overlying skin and fascia followed by isolation of the TA muscle through severance of the distal TA tendon and surgical separation of the lower TA from surrounding muscle groups. The distal tendon was secured to a K1000 force transducer (Harvard Apparatus) *via* a 6–0 silk suture. A custom nerve cuff was placed on the deep peroneal nerve and the TA muscle was stimulated by a GRASS S48 Stimulator. Throughout the testing, the mouse and TA muscle were kept warm with an overhead heat lamp and TA muscle hydration was maintained through regular application of warmed saline. The initial pulse duration and frequency of the stimulator were set to 0.5 ms and 140 Hz, respectively, for adjustment of the stimulation voltage for maximum muscle contraction, typically 6–10 V. Optimal muscle tension, which is proportional to optimal muscle length, was determined in a subset of uninjured mice (N = 5 legs). Using the established stimulation voltage and a frequency of 1 Hz to elicit a muscle twitch response, as described in literature,[38–40] an optimal passive tension of 5 cN was established. This was done by evaluating the passive tension-active twitch force relationship for 1 to 9 cN of passive tension, with one-minute rest periods between each contraction. Using the optimal stimulation voltage and 5 cN of passive tension, the muscle was stimulated at increasing frequencies (60 to 140 Hz) until a maximum tetanic contraction was reached, typically 80 Hz. One-minute rest periods were maintained between each contraction. Contractions were registered as an output voltage using LabChart software v8.1.19. The output voltage was normalized to the baseline voltage prior to stimulation and converted to force using the transducer's conversion factor (eqn (1), $N \geq 3$ each group). Muscle physiology data points were excluded if the muscle response was abnormal. Abnormality was defined as signs of muscle exhaustion, nerve injury, or a defective nerve cuff (*e.g.*, oddly small or decreasing response over time), an irregular contraction shape in the voltage response curve, or an atypical muscle length to muscle force relationship. Grubb's outliers were not assessed. After force evaluation, the anesthetized mouse was euthanized using 1% carbon dioxide and cervical dislocation.

$$\text{Force} = (\text{Maximum output (V)} - \text{baseline output (V)}) \times 50\,\text{gram force per volt} \times 0.0098\,\text{Newton per gram force} \quad (1)$$

Histological analysis of muscle morphometrics and regeneration

On day 28 post-VML injury, mice were euthanized using carbon dioxide overdose and cervical dislocation. The injured left and uninjured right TA muscles were excised and weighed prior to fixation on a rocker in 0.2% PFA at 4 °C overnight. The mass of each corresponding left and right muscle was compared to calculate the muscle mass ratio. Following fixation, muscles were saturated with 20% sucrose (w/v) to achieve density equilibrium, and then embedded for cryo-sectioning in optical cutting temperature compound and snap frozen. 10 μm thick transverse tissue sections were stained with routine Hematoxylin & Eosin (H&E) or Masson's Goldner trichrome staining to evaluate tissue histomorphology. Brightfield images were taken by Oregon Health & Science University's Advanced Light Microscopy Core at 20× using the Zeiss Axioscan Slide Scanner. Collagen deposition was quantified using a combination of custom MATLAB code and the

Color Deconvolution tool in ImageJ. Firstly, Masson's Goldner images were preprocessed using the MATLAB code to subtract image background. The cleaned images were then opened in ImageJ and underwent Masson's Trichrome Color Deconvolution, a technique for unmixing brightfield images into channels which represent the absorbance of specific dyes. Collagen deposition was isolated by adjusting the threshold of the deconvolved red channel. The area of collagen deposition was then expressed as a percentage of the total muscle area ($N \geq 4$ each group).

For immunohistochemistry, tissues sections underwent further fixation with 4% PFA for 10 minutes, followed by permeabilization in 0.1% Triton-X 100 for 15 minutes, and blocking in 1% BSA for 30 minutes. Quantification of myofiber regeneration was performed using immunofluorescent staining with rabbit anti-laminin (1 : 100, overnight, 4 °C, Abcam), a basement membrane protein, that was then conjugated to goat anti-rabbit Alexa Fluor 594 (1 : 200, 1 hour, room temperature, Invitrogen) ($N \geq 3$ each group). The GFP+ myofibers from the EM were identified *via* staining with an anti-GFP polyclonal antibody (1 : 200, overnight, 4 °C, pre-conjugated to Alexa Fluor 488, Invitrogen) as without the addition of the antibody, GFP+ visualization was sparse ($N \geq 5$ each group). Tissues were mounted using VectaShield with DAPI (Vector Laboratories). All images were taken using a Zeiss LSM 900 confocal microscope and tiled *z*-stacked 20× images were used to capture the entire tissue cross-section. Newly regenerated myofibers were identified as cells with borders positive for laminin staining and with centrally located nuclei. To effectively capture regeneration, a region of interest (ROI) was masked for each tissue section which extended 500 μm from the border of the EM or 500 μm from the geometric center of the transverse tissue section if the animal did not receive an EM treatment. New myofiber density is expressed as the total number of myofibers with centrally located nuclei per square millimeter. Within the ROI, myofiber percent area, total myofiber count, and individual myofiber area were quantified using Cellpose 2.0.[41] The laminin channel was inserted into Cellpose and a custom model was run to segment each myofiber. The custom model was created using Cellpose's pre-trained "Cyto" model that was then fine-tuned using user input on 4 laminin training images. Masks of the segmented myofibers were saved and then overlayed on the original image ROIs in ImageJ using the Labels to ROIs plugin.[42] The area of each individual segmented myofiber was measured and then averaged for each animal. Additionally, the individual myofiber areas and myofiber counts were summed. The area occupied by myofibers was normalized to the defect site area ($N \geq 4$ each group).

Histological analysis of vascularity

Quantification of vascularity was performed using immunofluorescence staining with rat anti-CD31 (1 : 100, overnight, 4 °C, BD Biosciences), an endothelial marker, that was then conjugated to goat anti-rat Alexa Fluor 594 (1 : 200, 1 hour, room temperature, Invitrogen). Tissues were mounted using Vectashield with DAPI (Vector Laboratories). All images were taken using a Zeiss LSM 900 confocal microscope and tiled *z*-stacked 20× images were used to capture the entire tissue cross-section.

Blood vessels were quantified semi-automatically using ImageJ and Cellpose 2.0.[41] Briefly, in ImageJ, a ROI was created which extended 500 μm from the border of the EM or 500 μm from the geometric center of the transverse tissue section if the animal did not receive an EM treatment. The CD31 and DAPI channels were split and saved as grayscale images. The DAPI channel was inserted into Cellpose and a custom model was run to segment the cell nuclei. The custom model was created using Cellpose's pre-trained "Nuclei" model that was then fine-tuned using user input on 4 nuclei training images. Masks of the segmented nuclei were saved and then overlayed as ROI's on the CD31 channel image in ImageJ using the Labels to ROIs plugin.[42] The mean gray value of each ROI was measured and normalized to the background mean gray value. The background was taken from the average mean gray value of 10 background ROIs plus the standard deviation of those background ROIs. The addition of the standard deviation allowed for a more conservative estimate of the background fluorescence. The vascularization was expressed as vessel density, the total number of vessels per square millimeter, or as vessels per myofiber ($N \geq 3$ each group).

Histological analysis of muscle innervation

Quantification of muscle innervation was performed using immunofluorescent staining of neuromuscular junction (NMJ) markers rabbit anti-synaptophysin (1 : 100, overnight, 4 °C, Abcam) that was conjugated to goat anti-rabbit Alexa Fluor 488 (1 : 200, 1 hour, room temperature, Invitrogen) and anti-α-bungarotoxin (1 : 100, 45 minutes, room temperature, pre-conjugated Alexa 594, Invitrogen). NMJs were counted throughout the entirety of the TA muscle. The density of mature NMJs was quantified as the number of NMJ's positive for both α-bungarotoxin and synaptophysin per square millimeter ($N \geq 4$ each group). The density of NMJ's for each animal was averaged over four tissues each of which were approximately 50 μm apart.

Statistical analysis

All statistical analysis was completed using GraphPad Prism. When making comparisons between ages or between injured and contralateral controls, unpaired *T*-tests were utilized with or without Welch's correction depending on data variance unless the data was nonparametric, then a Mann–Whitney *T*-test was utilized. One-way ANOVA's with *post hoc* Tukey's adjustment were used to compare between experimental groups unless the data was nonparametric, then a Kruskal–Wallis test with *post hoc* Dunn's adjustment was performed. A repeated measures ANOVA was used to determine significance for the tension–force curve. Outliers were assessed using the Grubbs test unless otherwise specified. Significance was taken at $p < 0.05$ (*), $p < 0.01$ (**), $p < 0.001$(***), and $p < 0.0001$ (****). All graphs display mean ± standard deviation unless otherwise stated.

Results

In vitro characterization of engineered muscle

Engineered muscles (EM) were fabricated using a shear-based extrusion method to achieve aligned collagen nanofibrillar scaffolds which were then seeded with GFP+ primary mouse myogenic cells (Fig. 1A). Prior to cell seeding, the biophysical properties of the scaffolds were characterized by scanning electron microscopy. The collagen scaffolds had an average porosity of 11.3 ± 1.03% and contained highly aligned nanofibrils that exhibited an overall average anisotropy value of 0.804 ± 0.032 (Table 1). An anisotropy value approaching one denotes alignment lengthwise along the scaffold. Purity of the primary myogenic cell population was established prior to scaffold seeding using immunofluorescent staining with MyoD, an early myogenic marker (Fig. 1B). Cells positive for MyoD accounted for 84 ± 2.9% of the cell population. The percentage of myogenic cells was significantly greater than other MyoD- cells found within the culture (16 ± 2.9%, $p < 0.0001$) (Fig. 1C). This confirms the myo-

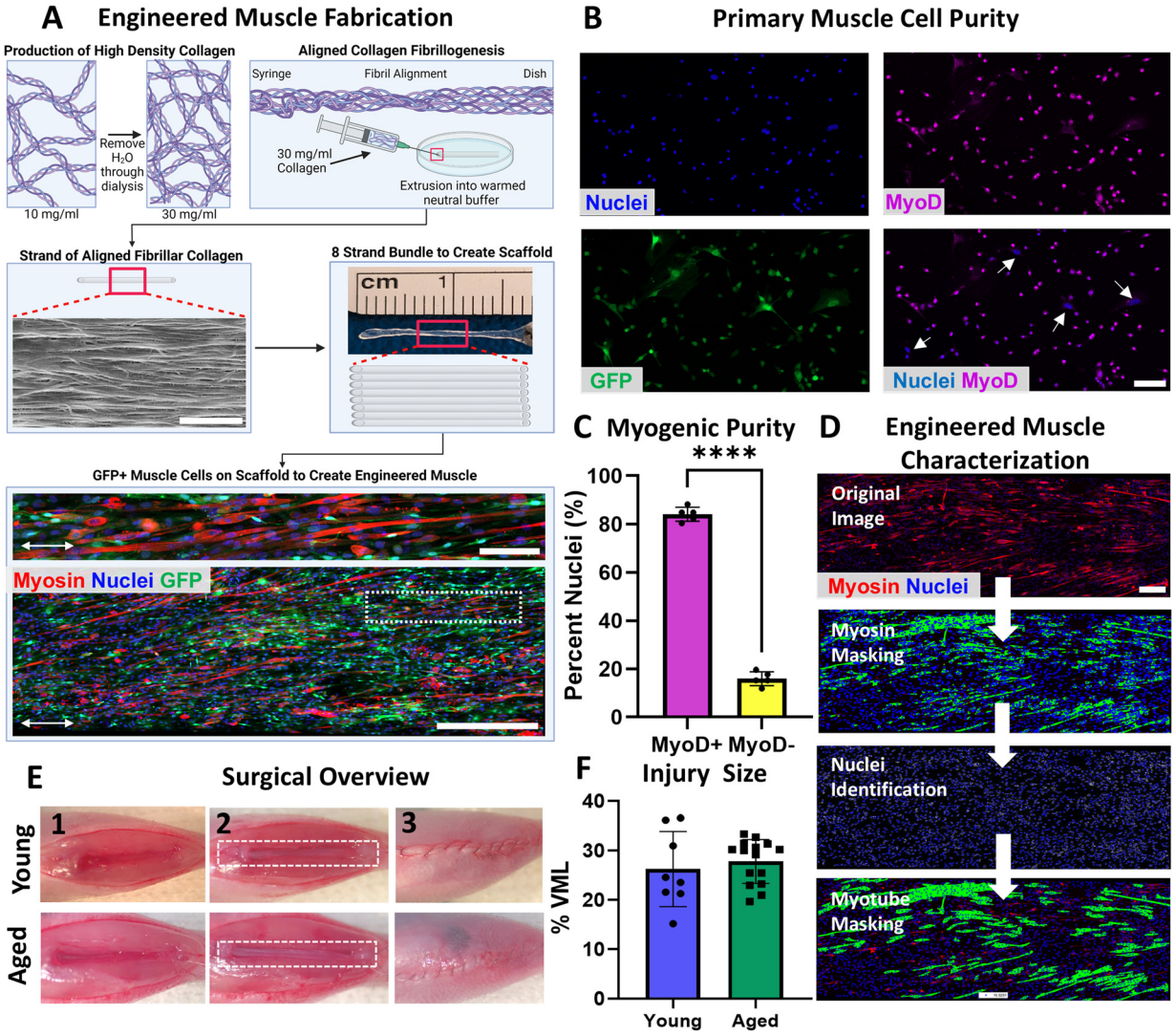

Fig. 1 Characterization of EM and model of murine VML. (A) Schematic demonstrating fabrication of the EM. Insets include a scanning electron microscopy image of aligned collagen nanofibrils which make up the structural foundation of the EM, a photograph of EM macrostructure, and confocal microscopy images of the EM at two different magnifications depicting immunofluorescent staining of MHC (red) and endogenous expression of GFP in differentiated myogenic cells (green). The arrow denotes the direction of collagen nanofibril orientation. (B) Confocal microscopy image of primary myogenic cells depicting MyoD, an early myogenic marker (magenta), DAPI, and endogenous GFP. Arrows denote non-myogenic cells. (C) Percentage of nuclei positive for MyoD in the primary cell population ($N = 5$). (D) Myotube analysis using MyoCount. From top to bottom images depict: identification of elements positive for MHC which exceed the set 'Tube Threshold', nuclear identification, and exclusion of MHC + structures with less than 3 nuclei (myoblasts). (E) VML surgical procedure in young (top) and aged mice (bottom) depicting (1) 20–30% TA muscle ablation, (2) EM implantation with EM denoted by white box, (3) muscle and skin closure over implanted EM. (F) Quantification of relative VML size between young and aged mice ($N \geq 8$). Scale bars: (A) 1 μm, 500 μm, 100 μm, (B) 100 μm, (D) 200 μm. Significance was determined using unpaired *T*-tests (C and F). Shown are mean ± SD.

Table 1 *In vitro* characterization of scaffold properties and engineered muscle. Average global porosity and anisotropy of collagen scaffolds (N = 3). Average myotube coverage and nuclear fusion index of myosin heavy chain-stained engineered muscles (N = 4). Shown are mean ± SD

SEM collagen fibril properties		Engineered muscle properties	
Porosity [%]	Anisotropy	Myotube area [%]	Nuclear fusion index [%]
11.3 ± 1.03	0.804 ± 0.032	17.6 ± 4.78	25.3 ± 5.67

genic purity of the primary cell population for use in the EM constructs.

After cell characterization, collagen scaffolds were seeded with GFP+ primary mouse myogenic cells which underwent differentiation into myosin-expressing myotubes to create the completed EMs. Immunofluorescent myosin heavy chain staining (MHC) and the presence of three or more nuclei were used to identify myotubes using MyoCount (Fig. 1D).[36] EM myotube coverage accounted for 17.6 ± 4.78% of the total construct area and EMs demonstrated an average nuclear fusion index (nuclei within myotubes compared to total nuclei) of 25.3 ± 5.67% (Table 1).

VML model characterization and validation

To evaluate how aging influences the efficacy of regenerative rehabilitation treatments following lower extremity injury, a skeletal muscle defect was surgically created in the tibialis anterior (TA) muscle of both young and aged mice (Fig. 1E). For a muscle injury to be representative of a VML injury, a greater than 20% initial loss of muscle mass is required.[1] To validate the size of the VML injury, the mass of the excised portion of the TA muscle at the time of surgery was compared to the mass of the contralateral control TA muscle at the study end point. There were no significant differences in the relative size of the muscle injury between young and aged mice which averaged between 26.2 ± 7.63% and 27.8 ± 4.44%, respectively (Fig. 1F). This data provides validation that the muscle injury in both the young and aged mice can be classified as a true VML injury. Following the induction of a VML injury in young and aged mice, animals were further divided into cohorts that received different rehabilitation regimens (exercise *versus* no exercise) or a combinatorial treatment with both exercise and an engineered muscle (Fig. 2A and B).

Age-dependent running activity

In addition to the treatment of the muscle defect with an EM, mice were given access to free running activity wheels between days 7 and 28 post-surgery (Fig. 2B and C). Animals were acclimated to the running wheels for three days prior to surgery and the distance run during the final 24 hours of acclimation was taken as individual baseline activity. Equal numbers of high and low runners were distributed evenly between the two exercise groups for each age: exercise alone (Y_{Ex}, A_{Ex}) and a combination treatment of both exercise and an engineered muscle (Y_{Ex+EM}, A_{Ex+EM}).

Within each age group, the average baseline running distance was similar between mice assigned to receive treatment with only exercise or exercise plus EM (young: $p < 0.69$, aged: $p < 0.43$). Following a recovery period of 7 days in static housing, all exercise groups returned to running activity that was comparable to baseline except for the aged group treated with exercise alone (A_{Ex}), which experienced a significant decrease in daily running distance (61 ± 28% of baseline distance, $p < 0.01$). Moreover, the normalized running distance of the A_{Ex} group was significantly lower compared to both young, exercised groups (Y_{Ex} and Y_{Ex+EM}, $p < 0.01$). These differences in short-term recovery suggest that youth as well as EM treatment promote an early return to normal activity while exercise alone is not sufficient in aged animals. By day 28 post-surgery, all groups exhibited similar running volumes compared to their baseline activity. Interestingly, the aged mice treated with exercise and EM (A_{Ex+EM}) and young mice treated with exercise only (Y_{Ex}), demonstrated a significant increase ($p < 0.05$) in daily running distance above baseline (Fig. 2D). These findings indicate a potential progressive benefit to exercise training in achieving greater fitness post injury.

While all groups roughly maintained a running distance equivalent to their baseline, a 2.6-fold stratification in total daily running distance between young and aged mice was maintained throughout the course of the study ($p < 0.001$) (Fig. 2E). Additionally, throughout the study, young and aged mice exhibited similar daily longest rest periods lasting approximately 6.6 hours (Fig. 2F), likely coinciding with the sleep cycle of the mouse. However, consistent with running distance, overall, young mice ran longer each day (1.8-fold, $p < 0.0001$), engaged in more frequent (1.4-fold, $p < 0.001$) and longer individual running bouts (1.7-fold, $p < 0.001$), had shorter rest periods between each running bout (1.5-fold, $p < 0.05$), and achieved higher average velocities (1.5-fold, $p < 0.05$) compared to aged mice (Fig. 2G–K). The comparative activity of young and aged mice indicates that self-selected running intensities decrease with age but eventually recover to or above baseline levels after several weeks of exercise post-VML. Additionally, these findings suggest that treatment with EM in the aged group led to greater running activity.

Quantification of muscle functional recovery

To evaluate functional muscle recovery following treatment of the VML injury, the maximum isometric force of the TA muscle was obtained during *in situ* muscle physiology. The TA muscle was stimulated *via* the peroneal nerve with increasing electrical frequencies until a maximum contraction was reached (Fig. 3A). The optimal passive muscle tension, which is equivalent to the optimal muscle length for evaluating active muscle force, was determined to be 5 cN. This determination was based on measurements of active muscle twitch force across a range of passive tensions from 1 to 9 cN, as well as supportive literature.[38] From 1 cN to 3 cN, active muscle twitch force significantly increased by 31.6 mN from 119 ± 5.45 mN to 151 ± 15.9 mN. However, beyond 3 cN, the passive tension-active force relationship began to plateau with incremental

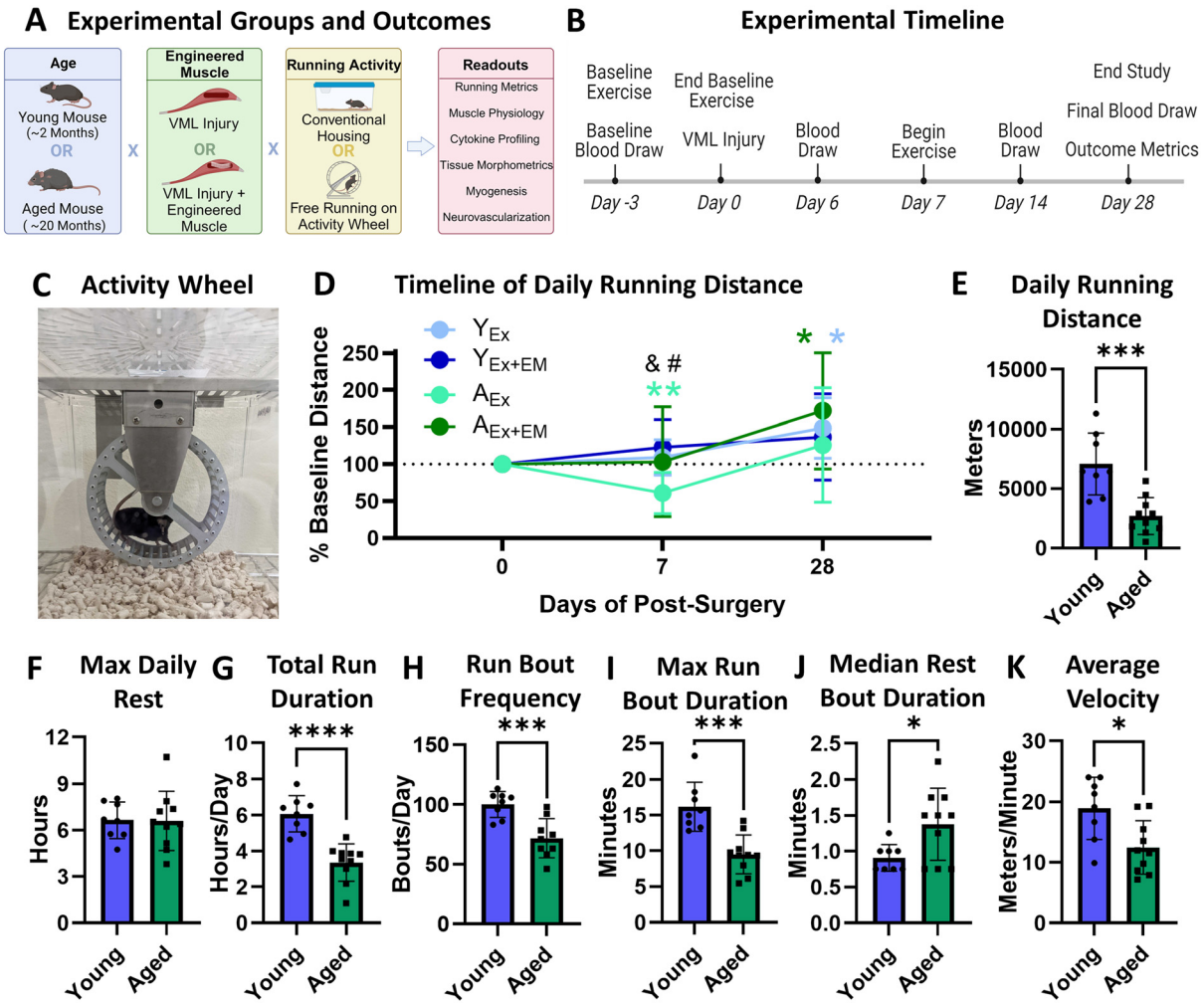

Fig. 2 Experimental overview and characterization of running activity between young and aged mice. (A) Schematic overview of experimental design depicting division into 6 groups based on mouse age, EM treatment, and exercise treatment. (B) Study timeline for collection of baselines, induction of injury, exercise onset/duration, and blood collection. (C) Photograph of mouse on an activity wheel. (D) Average daily running distance as a percent of baseline distance for each group that received exercise (Ex) on the final day of baseline exercise (day 0) and the first (day 7) and final (day 28) days of post-surgery exercise. Significance is demarcated relative to baseline (*) and relative to A_{Ex} and Y_{Ex} (#) and A_{Ex} and Y_{Ex+EM} (&) ($N \geq 8$ each group, each timepoint). Bar graphs depicting average (E) daily running distance, (F) longest daily rest period, (G) daily running duration, (H) daily running bout frequency, (I) longest running bout, (J) median rest length between running bouts, and (K) velocity of young (blue) and aged (green) mice averaged over the 21-day exercise program ($N \geq 8$). Significance was determined using a Two-Way ANOVA (D) or an unpaired *t*-test with or without Welch's correction depending on data variance (E–K) with $p < 0.05$ (*), $p < 0.01$ (**, &, or #), $p < 0.001$ (***), and $p < 0.0001$ (****). Shown are mean ± SD.

non-statistically significant active force changes of 9.1, 2.7, and 0.4 mN from 3–5, 5–7, and 7–9 cN of passive tension, respectively (Fig. 3B). Given that the passive tension-active force relationship plateaued most dramatically around 5 cN, this passive tension was selected for muscle physiology testing.

The maximum isometric contraction was determined from the voltage response curves of tetanic stimulation and revealed that the muscle function of injured untreated mice, did not fully recover to the level of an uninjured contralateral TA muscle 28 days post-injury ($p < 0.01$ for young mice and $p < 0.001$ for aged mice) (Video S1, ESI Fig. 1A and B†). This persistent functional deficit further validates the critically sized nature of the VML injury model. Additionally, the force production of the uninjured contralateral limb was unaffected by age or treatment (ESI Fig. 1C†).

As a whole, the tetanic curves of young animals displayed greater amplitudes compared to treatment-matched aged animals (Fig. 3C). Interestingly, age had a significant impact on the recovery of muscle function in response to treatment with EM and exercise. Young mice showed a progressive increase in muscle force of the injured TA muscle with the addition of treatments. Treatment with exercise alone in young mice demonstrated a 1.54-fold increase in muscle force (180 ± 27 mN) compared to age-matched controls (117 ± 32 mN). Furthermore, when exercise was paired with a transplanted EM, function was significantly improved by 2.45-fold (286 ±

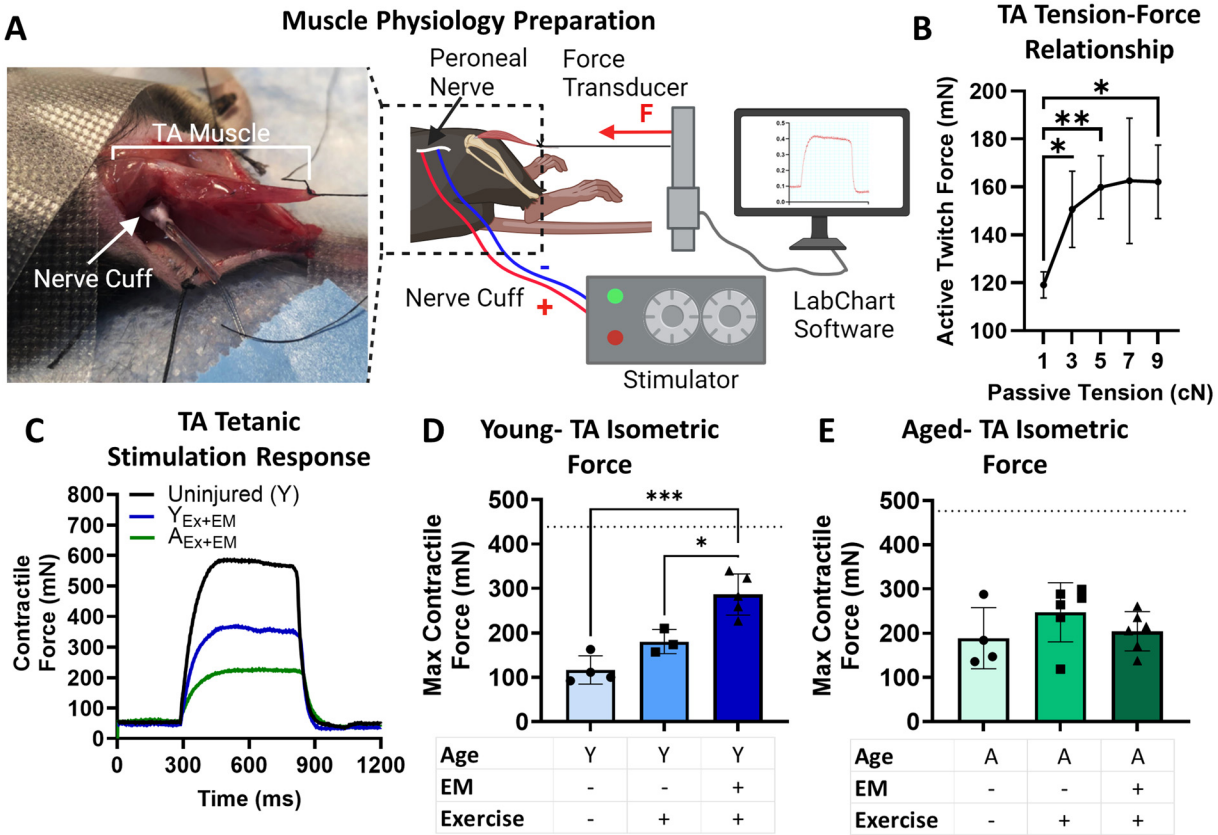

Fig. 3 Functional muscle force production in young (Y) and aged (A) mice treated with EM and rehabilitative exercise. (A) Surgical preparation and schematic overview of *in situ* muscle physiology testing *via* peroneal nerve stimulation. (B) Establishment of an optimal passive muscle tension of 5 cN using a passive tension-active force relationship curve. (C) Representative graph of tetanic voltage curves for a young uninjured TA muscle (black), a young TA muscle treated with EM and exercise (blue), and an aged TA muscle treated with EM and exercise (green). (D and E) Maximum contractile force of the injured TA muscle in young (D) and aged (E) mice in the presence (+) and/or absence (–) of EM and exercise ($N \geq 3$). The dashed line denotes the average contractile force of the contralateral control for each age group. Significance was determined using a repeated measures ANOVA (B) and a One-Way ANOVA (D and E) with $p < 0.05$ (*), $p < 0.01$ (**), and $p < 0.001$(***). Shown are mean ± SD.

46 mN, $p < 0.001$) (Video S2†) compared to the age-matched controls and by 1.59-fold ($p < 0.05$) compared to the exercise only group, respectively (Fig. 3D). In contrast, aged mice did not show any significant improvements in TA muscle force following treatment with exercise (247 ± 67 mN) or the combination of exercise paired with a transplanted EM (204 ± 44 mN) compared to age-matched controls (189 ± 69 mN) (Fig. 3E, and Video S3†). These findings demonstrate an additive functional benefit of coupling EM with exercise in young mice to improve muscle force recovery that was not mirrored in aged mice.

Muscle morphometrics and myogenesis

TAs were excised on the final day of the study (28 days post-surgery) and evaluated for size, mass ratio, and histology. H&E-stained tissue cross-sections revealed that treatment with EM and exercise increased TA muscle area in young but not aged mice (Fig. 4A). This increase in muscle size was validated by comparing muscle mass ratios (Fig. 4B and C), where the injured TA mass was compared to the contralateral uninjured TA mass. While exercise alone did not produce significant differences in mass ratio, the further addition of EM significantly increased the muscle mass ratio in young (0.70 ± 0.063, $p < 0.05$) but not aged (0.53 ± 0.023) mice compared to the age-matched exercise only and no treatment control groups (Fig. 4B and C). Masson's Goldner staining demonstrated similar collagen content, 13–22% of the TA area, across all treatments and ages (Fig. 4D–F). This suggests that the observed increase in mass ratio with the EM treatment in young mice was not associated with increases in fibrotic matrix deposition. Taken together, these data demonstrate additive improvements in mass recovery by coupling EM with exercise in young mice that again, was not mirrored in aged mice.

To determine if the age-specific differences in mass ratios could be due to attenuated myogenesis, the density of *de novo* myofibers, myofiber percent area, total myofiber count, individual myofiber cross sectional area (CSA), and the number of GFP+ transplanted cells were quantified. Immunofluorescent laminin staining was used to map individual myofiber boundaries, and myonuclear relocation (centrally located nuclei) was used as an indicator for actively regenerating *de novo* myofi-

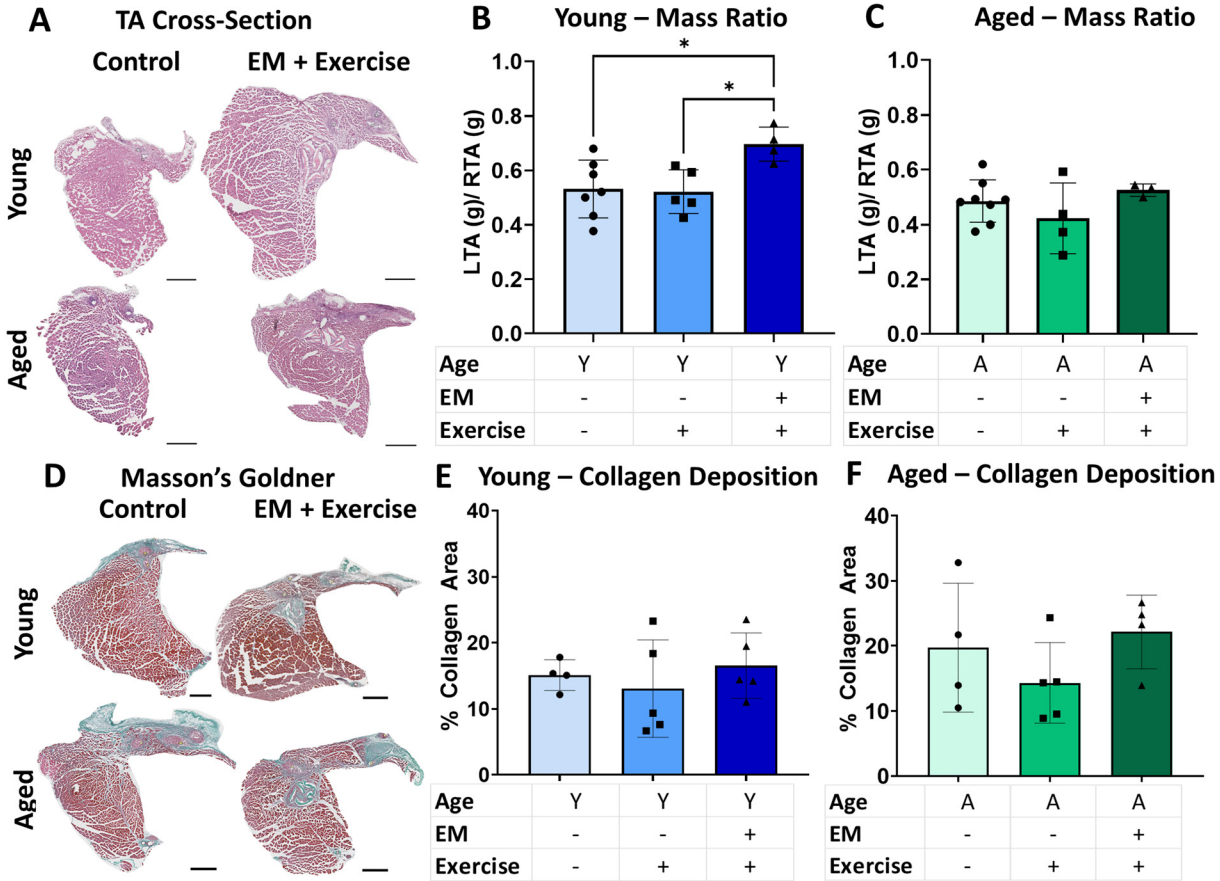

Fig. 4 TA muscle morphometrics and fibrosis following VML injury and treatment with EM and exercise. (A) Representative H&E staining of transverse TA muscle sections from untreated controls and mice that received both EM and exercise in both age groups. (B and C) Mass ratio of the injured left TA muscle (LTA) to the uninjured right TA muscle (RTA) in the young (B) and aged (C) groups in the presence (+) and/or absence (–) of EM and exercise ($N \geq 3$). (D) Representative Masson's Goldner staining of transverse TA muscle sections from untreated controls and mice that received both EM and exercise in both age groups. (E and F) Percent area positive for collagen relative to TA size in the young (E) and aged (F) groups in the presence (+) and/or absence (–) of EM and exercise ($N \geq 4$). Scale bars: (A and D) 500 μm. Significance was determined using a One-Way ANOVA with $p < 0.05$ (*). Shown are mean ± SD.

bers. Myofiber percent area, myofiber count, and myofiber CSA, secondary indicators of myogenesis, were assessed using Cellpose, a cellular segmentation algorithm, and the ImageJ plugin, Labels to ROIs (Fig. 5A).[41] Within the defect site (500 μm radius around the EM region or TA injury site), the density of *de novo* myofibers increased by 1.55-fold for young (383 ± 170 *de novo* myofibers per mm^2) and 1.62-fold for aged mice (539 ± 147 *de novo* myofibers per mm^2, $p = 0.088$) when treated with EM and exercise compared to age-matched controls (Fig. 5B and C).

In addition to analyzing *de novo* myofibers within the defect site, each site was assessed for secondary indicators of myogenesis. The percentage of the defect area covered by myofibers was not statistically different between all groups, ranging from 55.5% to 70.7% (ESI Fig. 2A and B†). However, a significant ($p < 0.05$) increase in the total number of myofibers was seen in young mice treated with exercise and EM (1.63-fold), and in aged animals that received only exercise (1.82-fold) compared to aged-matched controls (ESI Fig. 2C and D†).

The consistent myofiber percent area and the increased myofiber count complement the decrease in individual myofiber CSA following treatment with EM and exercise. Myofiber CSAs were significantly smaller in both young (665 ± 136 μm^2, $p < 0.05$) and aged mice (492 ± 80 μm^2, $p < 0.01$) compared to their corresponding controls (young: 1558 ± 582 μm^2; aged: 1019 ± 281 μm^2) (Fig. 5D and E). The frequency distribution of myofiber CSAs showed a pronounced shift towards smaller myofibers in all treatment groups compared to no treatment controls, which is consistent with an increased proportion of newly formed and actively regenerating myofibers (Fig. 5F and G). While EM and exercise treatment in both young and aged groups demonstrated greater *de novo* myofibers compared to their no-treatment controls, the slightly larger CSA of myofibers in the young group demonstrate greater hypertrophy, a common indicator of myofiber maturation.

The contribution of the transplanted myogenic cells on the EM was assessed by using anti-GFP immunofluorescence

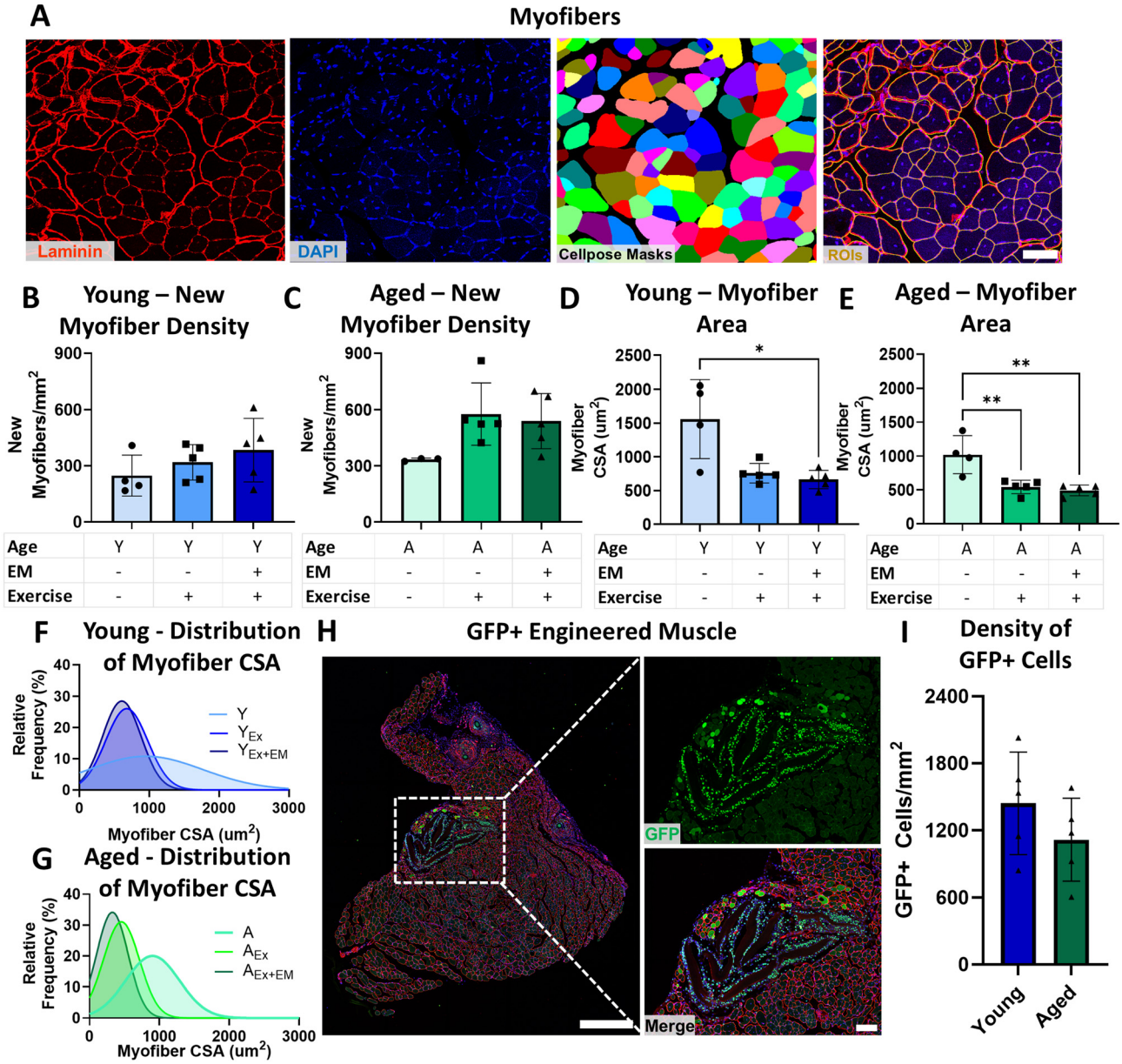

Fig. 5 Myogenesis following VML and treatment with EM and exercise. (A) Confocal microscopy of a transverse cross section of TA muscle depicting myofibers outlined by laminin (red) and overlayed with Cellpose masks or ImageJ ROIs of segmented myofibers. (B and C) Quantification of myogenesis from the density of myofibers with centrally located nuclei within a 500 μm area from the EM or TA injury site in the young (B) and aged (C) groups in the presence (+) and/or absence (–) of EM and exercise ($N \geq 3$). (D and E) Quantification of myofiber cross-sectional area (CSA) within a 500 μm area from the EM region or TA injury site in the young (D) and aged (E) groups in the presence (+) and/or absence (–) of EM and exercise ($N \geq 4$). (F and G) Frequency distributions of myofiber CSAs within a 500 μm area from the EM region or TA injury site in the young (F) and aged (G) groups in the presence (+) and/or absence (–) of EM and exercise. (H) Confocal microscopy of a transverse cross section of TA muscle with insets enlarging the region surrounding the EM. Staining depicts myofibers outlined by laminin (red) with GFP+ myofibers originating from the EM (green). (I) Density of GFP+ myofibers within the EM and the surrounding 100 μm in young and aged mice ($N \geq 5$). Scale bars: (A) 50 μm, (H) 500 μm (left) and 100 μm (right). Significance was determined using a One-Way ANOVA or a Kruskal–Wallis test for nonparametric data (B–E) and an unpaired *t*-test (I). Shown are mean ± SD.

staining of tissue sections to visualize the GFP labeled cells (Fig. 5H). The presence of transplanted GFP+ cells was examined within a restricted radius around the defect site (100 μm radius around the EM region) as cells originating from the EM were not expected to extend far past the EM. The density of GFP+ cells was similar between the young (1443 ± 459 cells per mm^2) and aged mice (1117 ± 371 cells per mm^2) (Fig. 5I). The majority of GFP+ cells were localized within the EM, indicating overall limited engraftment of the EM with the surrounding tissue.

Muscle vascularization and innervation

Re-vascularization and innervation within the injured muscle are key first steps in supporting proper muscle healing. Blood vessels were identified semi-automatically using ImageJ and Cellpose[41] by colocalization of nuclear regions identified with DAPI staining with the endothelial marker, CD31 (Fig. 6A). Young mice treated with EM and exercise experienced significantly greater vascular regeneration marked by a 2-fold greater density of blood vessels (2209 ± 394 blood vessels per mm^2) compared to aged-matched controls (1156 ± 42.8 blood vessels per mm^2, $p < 0.01$) or treatment with just exercise alone (1550 ± 210 blood vessels per mm^2, $p < 0.05$) (Fig. 6B). However, blood vessel density of the aged mice was similar across all groups (Fig. 6C). Although treatment did not alter the ratio of vessels per myofiber in young mice, the addition of exercise decreased the vessel-to-myofiber ratio in aged mice (1.73 ± 0.159 vessels per myofiber, $p < 0.01$) (Fig. 6D and E) compared to age-matched controls. The number of vessels per myofiber was also upwards of 1.35-fold higher in young mice compared to treatment-matched aged mice.

Innervation was evaluated across the entire TA muscle cross-sectional area and averaged across multiple tissue sections for each animal to account for the inherent variable clustering of neuromuscular junctions (NMJ). NMJs were identified *via* the colocalization of α-bungarotoxin (red) and synaptophysin (green) (Fig. 6F). Regardless of treatment, NMJ density was similar within each age group. However, for both young and aged mice, treatment with EM and exercise moderately increased the density of NMJs by 1.2-fold (5.36 ± 0.45 NMJs per mm^2) and 1.4-fold (5.29 ± 2.75 NMJs per mm^2), respectively, compared to aged-matched controls (Fig. 6G and H). Taken together, young animals treated with both EM and exercise demonstrated a significant increase in vascular density and both age groups experienced a moderate increase in innervation.

Systemic cytokine and chemokine profiles

Systemic cytokine and chemokines levels were evaluated over the course of the study through plasma samples taken at baseline (prior to surgery) and at 1-, 2-, and 4-weeks post-surgery (Fig. 2B). Cytokine and chemokine data was *z*-scored and plotted on a clustered heatmap based on treatment and timepoint (Fig. 7A). The heatmap revealed no sizable clusters based on timepoint, treatment, or age. Within age groups, treatment with EM and exercise had limited overall effect on systemic cytokine levels over the course of the study. Line graphs of logarithmically transformed values of mean fluorescent intensity (MFI) data for select cytokines illustrate the absence of temporal alterations in cytokine level (Fig. 7B). For each age group, cytokine levels were similar across all timepoints and treatments. However, aged mice had significantly higher baseline levels of Eotaxin ($p < 0.0001$), IL-7 ($p < 0.01$), LIF ($p < 0.001$), IL-15 ($p < 0.01$), and MIG ($p < 0.001$) compared to young mice prior to surgery (Fig. 7C). These cytokines remained elevated in the aged mice throughout the full duration of the study suggesting chronic alteration in cytokine levels due to aging (Fig. 7D). These findings may also implicate age-related inflammation as a mediator of tissue response to regenerative rehabilitation treatments following VML.

Discussion

The most persistent clinical challenges facing treatment and recovery from severe volumetric muscle loss (VML) injuries continue to be functional healing and improved quality of life. Surgical and physical management of VML as well as the regenerative tissue response varies greatly between patients and much remains unknown on how to best optimize therapeutic outcomes. Regenerative treatments have emerged that facilitate improved healing through the combination of engineered therapies and physical rehabilitation; however, many of these approaches have been evaluated in the absence of age heterogeneity. By leveraging preclinical models of regenerative rehabilitation within an age-diverse setting, a clearer and more complete picture of muscle healing emerges that shows divergent roadmaps for success.

The current study utilized engineered muscle (EM) consisting of a patterned nanofibrillar collagen scaffold laden with differentiated myogenic cells in combination with voluntary wheel running to provide a combinatorial regenerative treatment following VML injury in young and aged mice. Through this dual treatment model, the regenerative response to an engineered therapy and physical rehabilitation could be evaluated independently and in combination. Young (8 weeks) and aged (80 weeks) mice that roughly parallel human ages of 18 and 60 years,[37] respectively were used to assess the influence of age on the effectiveness of these combined therapies in the restoration of muscle function following VML.

Age-specific differences in muscle regeneration and function were evident in both histological and functional evaluations. Young animals that were treated with both EM and exercise experienced a significant increase in muscle mass ratio, muscle force production, and revascularization following VML injury compared to age-matched controls and animals that only received exercise without EM. The improvement in muscle structural, compositional, and functional outcomes highlights the regenerative potency of the combined treatment for young populations. These findings are consistent with prior work that has demonstrated a synergistic benefit of combining a regenerative biomaterial scaffold with running exercise.[11,13] However, aged animals did not have a similar healing response to the combined EM and exercise treatment, suggesting that this regenerative rehabilitation approach acts through age-specific pathways. There is likely a combination of age-related factors driving this diminished regenerative response including myogenic capacity, vascularization, endogenous inflammatory response, and overall systemic response to injury and exercise.

This study highlights the crucial role of age in driving therapeutic efficacy. Further investigation of EM as a thera-

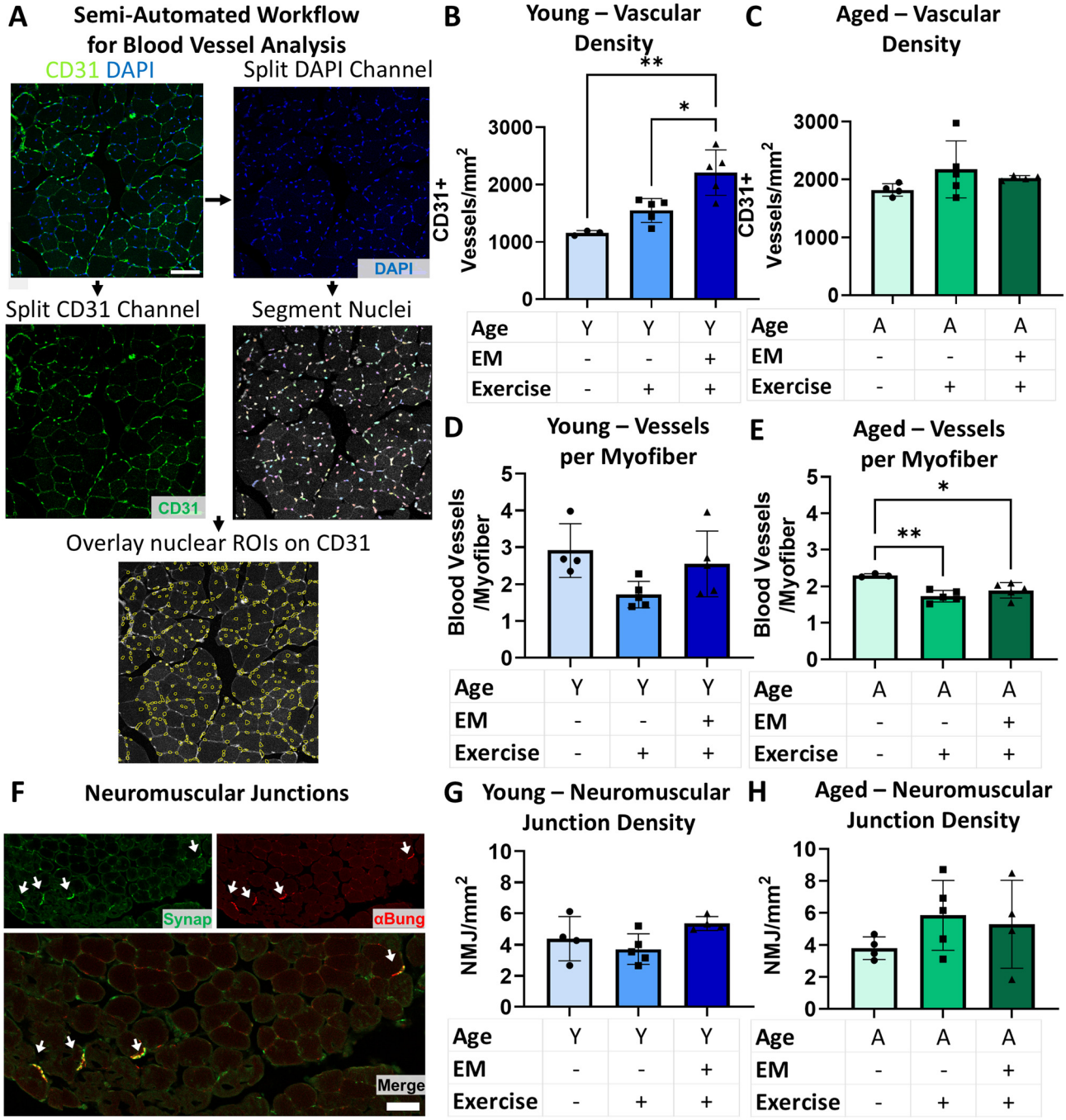

Fig. 6 Neurovascularization in the TA muscle following VML and treatment with EM and exercise. (A) Diagram of semi-automatic blood vessel quantification using Cellpose and ImageJ. Vessels were identified by colocalization of nuclear regions identified with DAPI staining (blue) with the endothelial marker, CD31 (green). (B and C) Quantification of vascular density within a 500 μm area from the EM or TA injury site in the young (B) and aged (C) groups in the presence (+) and/or absence (–) of EM and exercise ($N \geq 3$). (D and E) Quantification of blood vessels per myofiber within a 500 μm area from the EM or TA injury site in the young (D) and aged (E) groups in the presence (+) and/or absence (–) of EM and exercise ($N \geq 3$). (F) Confocal microscopy image of a transverse cross section of TA muscle depicting neuromuscular junctions (NMJ) co-stained with synaptophysin (Synap)(green) and alpha-bungarotoxin (αBung)(red). (G and H) Quantification of NMJ density within the entire TA muscle in the young (G) and aged (H) groups in the presence (+) and/or absence (–) of EM and exercise ($N \geq 4$). Scale bars: (A and F) 50 μm. Significance was determined using a One-Way ANOVA or a Kruskal–Wallis test for nonparametric data with $p < 0.05$ (*) and $p < 0.01$ (**). Shown are mean ± SD.

peutic could benefit from examining an engineered muscle-only group and exploring how donor cell age affects treatment outcomes. Previous studies[11,22] have shown that combining EM with exercise enhanced muscle regeneration compared to EM alone. Therefore, this study focused on the impact of age using the most effective therapeutic combination.

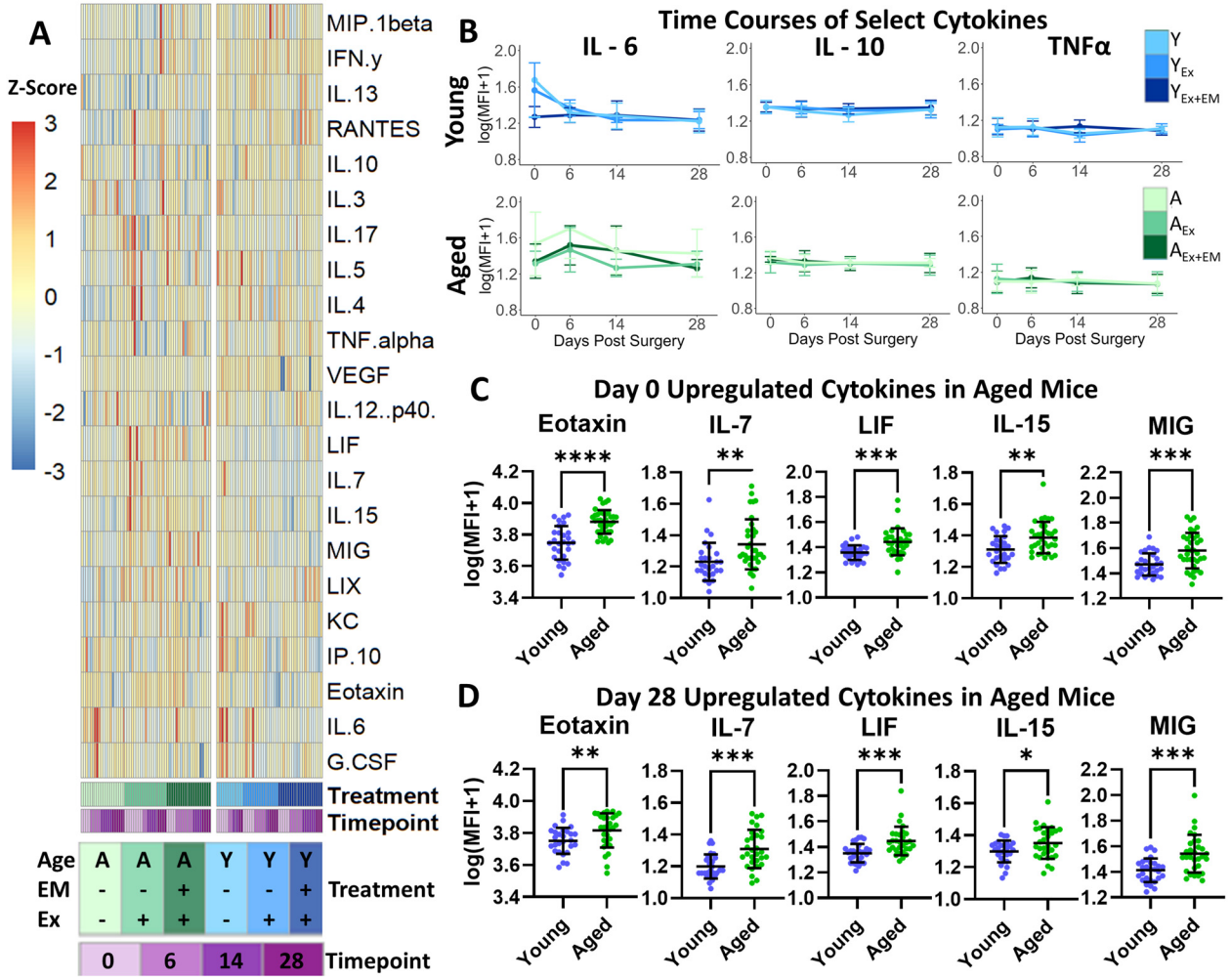

Fig. 7 Systemic cytokines profiles. (A) Heatmap of *z*-scored cytokine levels (columns) in all groups prior to surgery (Day 0) and at Days 6, 14, and 28 post-surgery. (B) Representative cytokine time courses presented as log transformed mean fluorescent intensities (MFI) following VML injury and treatment. (C) Bar graphs of the five cytokines which were upregulated between young and aged mice prior to surgery and (D) 28 days post-surgery ($N \geq 27$). Significance was determined using unpaired *T*-tests or Mann–Whitney *T*-tests for nonparametric data with $p < 0.01$ (**), $p < 0.001$(***), and $p < 0.0001$(****). Shown are mean ± SD.

Additionally, the goal of this study was to evaluate the therapeutic efficacy of adding regenerative therapies to a standard of care such as physical therapy, as the most feasible extension of current patient care. While future exploration of all therapeutic combinations is essential to build a more comprehensive picture of regenerative rehabilitation, it may not be immediately necessary until differential treatment responses are observed in aged animals.

For the fabrication of the EM, primary muscle cells were isolated from young (5-week-old) mice. While aged donor cells can be isolated, cells from young donors exhibit more efficient outgrowth and proliferation, which best supports EM fabrication.[33] Future studies should explore the use of donor cells from all ages, given that clinical applications may use autologous or allogenic cells, which must be effective regardless of donor age. Although donor age is an important factor, studies have shown that the transplant environment is a greater determinant of donor cell regenerative potential than donor age, particularly in muscle.[43] This suggests that aged donor cells can still promote regeneration when used for EM if transplanted into a younger individual. Moreover, it underscores that regulation of the environment surrounding the transplanted EM could be equally as important as the EM itself.

As the body and muscles age, myofibers increasingly exhibit impaired activation, reduced energy production, and contain fewer numbers of satellite cells, which reduces the fusion efficiency of myogenic cells to form new myofibers.[27,28] Newly formed myofibers frequently have smaller CSAs, due to a lack of sustained hypertrophy. The increase in the number of smaller myofibers in both age groups with the dual treatment suggests that there was a greater presence of actively regenerating and new myofibers. However, the greater force generation exhibited by the young muscles compared to the aged, suggests that the newly formed myofibers may have a reduced functional capacity in aged animals. Future work is needed to expansively characterize the fiber type and oxidative capacity of

these smaller myofibers to identify age-specific variations correlating type with contractile properties[44] to elucidate their role in aged healing. Additionally, age-related differences in myogenesis could be even further clarified by examining variations in histological staining or gene expression of myogenic-differentiation factors such as myosin heavy chain (MHC) and myoblast differentiation protein 1 (MyoD).[9,10]

Dense capillary beds within the muscle ensure the highly efficient transportation of nutrients, oxygen, and toxin removal to support the heavy metabolic needs of the tissue. Treatments that promote the vascularization of injured muscle are known to result in more robust myogenesis and functional recovery.[11–13,22] Extensive vascularization following VML injury was achieved in young animals that were treated with combined EM and exercise. However, exercise without EM treatment was less effective in improving vascularization in young mice suggesting that exercise alone lacks the additional pro-regenerative microenvironment provided by EM. The EM likely provides biophysical guidance that serves to stabilize and support injured muscle, facilitates force transmission to stimulate blood flow, and produces local regenerative cytokines. While the exact mechanosensitive pathways remain unknown, exercise plays a synergistic and complementary role to EM in directing a pro-regenerative environment.

The ratio of vessels-to-myofibers was consistently lower in aged mice compared to young mice that were given the same treatment. This difference is likely due, in part, to the overall smaller myofiber CSAs observed in aged mice as there is a positive correlation between myofiber size and capillary supply, regardless of age.[45] Although this study did not directly explore native vascularization, other studies suggest that lower initial vessel to myofiber ratios restrict the extent that muscle can adapt to external stimuli, such as exercise[46–49] and possibly EM. Additionally, elevated levels of dysregulating cytokines in the blood plasma, notably MIG which is known for its anti-angiogenic properties,[50,51] may be counteracting the angiogenic effects of EM and exercise in aged animals. Thus, in young populations, EM and exercise stimulated vascularization to support the metabolic demands of regenerating functional skeletal muscle, but age-related changes to vascularization may restrict the ability of skeletal muscle to respond to regenerative stimuli.

A well-controlled inflammatory response is a critical component of effective wound healing to mediate functional tissue remodeling. However, chronic inflammation associated with aging is disruptive to musculoskeletal regenerative programs and may interfere with the effectiveness of regenerative therapeutics. In this study, five cytokines/chemokines, MIG (CXCL9), IL-7, IL-15, Eotaxin (CCL11) and LIF, were elevated in the plasma of aged mice at baseline and continued to be elevated post-injury compared to young mice, indicating chronic elevation of these factors. Out of these factors, MIG and IL-7 are classically pro-inflammatory and anti-myogenic[52–55] and their chronic upregulation may have contributed to the inhibition of muscle recovery post-VML in aged mice. Conversely, Eotaxin and LIF are known regenerative cytokines.[56–58] However, their consistent upregulation, observed here and in other cases of aging and disuse,[59–61] hints at a compensatory mechanism aimed at mitigating age-related muscle loss. Future work should locally examine these age-related cytokines, among others, such as IL-6,[9,10] to better understand their direct interaction with muscle during regeneration and in response to exercise and transplanted constructs. Cytokine heterogeneity in aged mice presents a challenge for controlling the regenerative response to rehabilitation exercise as both are highly complex and interwoven with the immune state. However, these studies involved a small sample size which may have contributed to some of the cytokine heterogeneity. The future landscape of regenerative rehabilitation is likely to involve a strategically balanced conversation between pro- and anti-regenerative responses.

While it is well-established that exercise stimulates many local and systemic factors that contribute to muscle metabolism, hypertrophy, blood flow, and even activation of satellite cells,[62–64] the biological mechanism responsible for synergizing with EM is still only predictive. In the current study, voluntary wheel running was used to simulate aerobic exercise, which allowed animals to self-select for running intensity in accordance with age, mirroring differences in clinical regimens prescribed to young and aged individuals during physical therapy. Moreover, this exercise strategy reduced the likelihood of aged animals experiencing exercise-induced overuse injuries, as exercise tolerance decreases with age.[65] However, with exercise self-selection, a threshold for facilitating synergistic benefits of exercise combined with EM may not have been achieved in aged animals, potentially contributing to their lack of improved regenerative outcomes. In addition to optimizing for aerobic exercise intensity, other exercise modalities such as resistance training may be better suited for aged populations. While a universal physical therapy regimen that synergizes with engineered therapies would revolutionize recovery from musculoskeletal trauma, patient heterogeneity necessitates an age-tailored approach.

Conclusion

In summary, this study shows that combined regenerative rehabilitation strategies, such as engineered muscle and voluntary running exercise, are effective at facilitating functional muscle regeneration following VML in young but not aged populations. These findings implicate the need for broader evaluation of regenerative and rehabilitative strategies, tailored to age group, for treating musculoskeletal injuries and thus addressing a more inclusive patient demographic.

Author contributions

K.M.H. and K.H.N. conceived and designed the experiments. K.M.H., C.A.A., V.R.D., and Y.H.T. collected the data. K.M.H., V.R.D., Y.H.T., and K.H.N. analyzed the data. K.M.H. and K.H.

N. wrote the manuscript. N.J.W. designed the muscle physiology assessments. All authors provided editorial input on the manuscript.

Data availability

The data that support the findings of this study will be available from the corresponding author upon reasonable request.

Conflicts of interest

There are no conflicts to declare.

Acknowledgements

We thank the Oregon Health & Science University Advanced Light Microscopy Core and Flow Cytometry Core for the use of shared equipment, services, and expertise. In addition, we thank Meghan Fallon for providing the MATLAB code for collagen analysis and Thomas Habing for his assistance in developing the C++ code for the exercise analysis. BioRender and GraphPad Prism were used for the creation of scientific illustrations in this publication.

This research was supported in part by funding from the Alliance for Regenerative Rehabilitation Research & Training, MTF Biologics, the Oregon Medical Research Foundation, and the Collins Medical Trust. K. M. H. was supported by the National Science Foundation Graduate Research Fellowship (DGE-1937961) and the Oregon Students Learn and Experience Research Program (5TL1TR2371-8). V. R. D. was supported by the National Institute of Dental and Oral and Craniofacial Research Training Award T90 (DE030859-03). K. H. N. was supported by grants from the NIH/NHLBI (R00HL136701) and NIH/NIAMS (R01AR080150); N. J. W. was supported by grants from the NIH/NIAMS (R01AR078375) and the Department of Veterans Affairs (5 I01 RX001985).

References

1 B. F. Grogan, J. R. Hsu and S. T. R. Consortium, *J. Am. Acad. Orthop. Surg.*, 2011, **19**, S35–S37.
2 S.-H. Lin, D. C.-C. Chuang, Y. Hattori and H.-C. Chen, *J. Reconstr. Microsurg.*, 2004, **20**, 227–235.
3 C.-H. Lin, Y.-T. Lin, J.-T. Yeh and C.-T. Chen, *Plast. Reconstr. Surg.*, 2007, **119**, 2118–2126.
4 M. Klinkenberg, S. Fischer, T. Kremer, F. Hernekamp, M. Lehnhardt and A. Daigeler, *Plast. Reconstr. Surg.*, 2013, **131**, 293–302.
5 B. T. Corona, J. C. Wenke and C. L. Ward, *Cells Tissues Organs*, 2016, **202**, 180–188.
6 B. J. Hurtgen, C. L. Ward, C. M. Leopold Wager, K. Garg, S. M. Goldman, B. E. P. Henderson, T. O. McKinley, S. M. Greising, J. C. Wenke and B. T. Corona, *Physiol. Rep.*, 2017, **5**, e13362.
7 G. Haas, A. Dunn, J. Madsen, P. Genovese, H. Chauvin, J. Au, N. Ziemkiewicz, D. Johnson, A. Paoli, A. Lin, N. Pullen and K. Garg, *J. Biomed. Mater. Res., Part A*, 2021, **109**, 2280–2293.
8 T. Huynh, C. Reed, Z. Blackwell, P. Phelps, L. C. P. Herrera, J. Almodovar, D. A. Zaharoff and J. Wolchok, *Sci. Rep.*, 2023, **13**, 1983.
9 M. Shi, R. Dong, J. Hu and B. Guo, *Chem. Eng. J.*, 2023, **457**, 141110.
10 M. Shi, L. Bai, M. Xu, R. Dong, Z. Yin, W. Zhao, B. Guo and J. Hu, *Chem. Eng. J.*, 2024, **484**, 149019.
11 K. H. Nakayama, C. Alcazar, G. Yang, M. Quarta, P. Paine, L. Doan, A. Davies, T. A. Rando and N. F. Huang, *npj Regener. Med.*, 2018, **3**, 16.
12 K. H. Nakayama, M. Quarta, P. Paine, C. Alcazar, I. Karakikes, V. Garcia, O. J. Abilez, N. S. Calvo, C. S. Simmons, T. A. Rando and N. F. Huang, *Commun. Biol.*, 2019, **2**, 170.
13 C. A. Alcazar, C. Hu, T. A. Rando, N. F. Huang and K. H. Nakayama, *Biomater. Sci.*, 2020, **8**, 5376–5389.
14 T. D. Brutsaert, T. P. Gavin, Z. Fu, E. C. Breen, K. Tang, O. Mathieu-Costello and P. D. Wagner, *BMC Physiol.*, 2002, **2**, 8.
15 M. D. Ross, A. L. Wekesa, J. P. Phelan and M. Harrison, *Med. Sci. Sports Exercise*, 2014, **46**, 16–23.
16 F. Ambrosio, R. J. Ferrari, G. Distefano, J. M. Plassmeyer, G. E. Carvell, B. M. Deasy, M. L. Boninger, G. K. Fitzgerald and J. Huard, *Tissue Eng., Part A*, 2010, **16**, 839–849.
17 T. M. Gregory, R. A. Heckmann and R. S. Francis, *J. Manip. Physiol. Ther.*, 1995, **18**, 72–78.
18 N. E. Gentile, K. M. Stearns, E. H. Brown, J. P. Rubin, M. L. Boninger, C. L. Dearth, F. Ambrosio and S. F. Badylak, *Am. J. Phys. Med. Rehabil.*, 2014, **93**, S79–S87.
19 K. Garg, C. L. Ward, B. J. Hurtgen, J. M. Wilken, D. J. Stinner, J. C. Wenke, J. G. Owens and B. T. Corona, *J. Orthop. Res.*, 2015, **33**, 40–46.
20 V. J. Mase, Jr., J. R. Hsu, S. E. Wolf, J. C. Wenke, D. G. Baer, J. Owens, S. F. Badylak and T. J. Walters, *Orthopedics*, 2010, **33**, 511.
21 V. Cheuy, S. Picciolini and M. Bedoni, *npj Regener. Med.*, 2020, **5**, 16.
22 M. Quarta, M. Cromie, R. Chacon, J. Blonigan, V. Garcia, I. Akimenko, M. Hamer, P. Paine, M. Stok, J. B. Shrager and T. A. Rando, *Nat. Commun.*, 2017, **8**, 15613.
23 I. o. Medicine, *Returning Home from Iraq and Afghanistan: Assessment of Readjustment Needs of Veterans, Service Members, and Their Families*, The National Academies Press, Washington, DC, 2013.
24 J. J. Lewis, D. Leung, J. Espat, J. M. Woodruff and M. F. Brennan, *Ann. Surg.*, 2000, **231**, 655–663.
25 M. Gaffley, A. A. Weaver, J. W. Talton, R. T. Barnard, J. D. Stitzel and M. R. Zonfrillo, *Traffic Inj. Prev.*, 2019, **20**, S63–S68.

26 Ç. Gemci, A. Imerci and N. H. Aydogan, *Cureus*, 2023, **15**, e44058.
27 G. Distefano and B. H. Goodpaster, *Cold Spring Harb. Perspect. Med.*, 2018, **8**, a029785.
28 N. Miljkovic, J. Y. Lim, I. Miljkovic and W. R. Frontera, *Ann. Rehabil. Med.*, 2015, **39**, 155–162.
29 S. D. Gopinath and T. A. Rando, *Aging Cell*, 2008, **7**, 590–598.
30 J. T. Kim, B. M. Kasukonis, L. A. Brown, T. A. Washington and J. C. Wolchok, *Exp. Gerontol.*, 2016, **83**, 37–46.
31 J. T. Kim, B. M. Kasukonis, G. Dunlap, R. Perry, T. Washington and J. Wolchok, *Tissue Eng., Part A*, 2020, **26**, 3–14.
32 J. T. Kim, K. Roberts, G. Dunlap, R. Perry, T. Washington and J. C. Wolchok, *J. Tissue Eng. Regener. Med.*, 2022, **16**, 367–379.
33 A. Shahini, K. Vydiam, D. Choudhury, N. Rajabian, T. Nguyen, P. Lei and S. T. Andreadis, *Stem Cell Res.*, 2018, **30**, 122–129.
34 C. Grove and D. A. Jerram, *Comput. Geosci.*, 2011, **37**, 1850–1859.
35 A. Boudaoud, A. Burian, D. Borowska-Wykręt, M. Uyttewaal, R. Wrzalik, D. Kwiatkowska and O. Hamant, *Nat. Protoc.*, 2014, **9**, 457–463.
36 D. P. Murphy, T. Nicholson, S. W. Jones and M. F. O'Leary, *Wellcome Open Res.*, 2019, **4**, 6.
37 K. Flurkey, J. M. Currer and D. E. Harrison, in *The Mouse in Biomedical Research*, ed. J. G. Fox, M. T. Davisson, F. W. Quimby, S. W. Barthold, C. E. Newcomer and A. L. Smith, Academic Press, Burlington, 2nd edn, 2007, pp. 637–672. DOI: **10.1016/B978-012369454-6/50074-1**.
38 C. H. Hakim, D. Li and D. Duan, *Methods Mol. Biol.*, 2011, **709**, 75–89.
39 C. H. Hakim, N. B. Wasala and D. Duan, *J. Visualized Exp*, 2013, **72**, e50183.
40 E. Verburg, H.-M. S. Thorud, M. Eriksen, N. K. Vøllestad and O. M. Sejersted, *Am. J. Physiol.: Regul., Integr. Comp. Physiol.*, 2001, **281**, R1952–R1965.
41 M. Pachitariu and C. Stringer, *Nat. Methods*, 2022, **19**, 1634–1641.
42 A. Waisman, A. M. Norris, M. Elías Costa and D. Kopinke, *Sci. Rep.*, 2021, **11**, 11793.
43 B. Carlson and J. Faulkner, *Am. J. Physiol.: Cell Physiol.*, 1989, **256**, C1262–C1266.
44 T. van Wessel, A. de Haan, W. J. van der Laarse and R. T. Jaspers, *Eur. J. Appl. Physiol.*, 2010, **110**, 665–694.
45 Y. Barnouin, J. S. McPhee, G. Butler-Browne, A. Bosutti, G. De Vito, D. A. Jones, M. Narici, A. Behin, J. Y. Hogrel and H. Degens, *J Cachexia Sarcopenia Muscle*, 2017, **8**, 647–659.
46 T. Moro, C. R. Brightwell, D. E. Phalen, C. F. McKenna, S. J. Lane, C. Porter, E. Volpi, B. B. Rasmussen and C. S. Fry, *Exp. Gerontol.*, 2019, **127**, 110723.
47 T. Snijders, J. P. Nederveen, S. Joanisse, M. Leenders, L. B. Verdijk, L. J. C. van Loon and G. Parise, *J. Cachexia, Sarcopenia Muscle*, 2017, **8**, 267–276.
48 M. W. Betz, T. Aussieker, C. Q. Kruger, S. H. M. Gorissen, L. J. C. van Loon and T. Snijders, *Exp. Gerontol.*, 2021, **143**, 111161.
49 B. E. Phillips, P. J. Atherton, K. Varadhan, M. C. Limb, D. J. Wilkinson, K. A. Sjøberg, K. Smith and J. P. Williams, *J. Physiol.*, 2015, **593**, 2721–2734.
50 C. Qi, X. Song, H. Wang, Y. Yan and B. Liu, *Front. Physiol.*, 2022, **13**, 981577.
51 C. W. Lee, E. Stabile, T. Kinnaird, M. Shou, J. M. Devaney, S. E. Epstein and M. S. Burnett, *J. Am. Coll. Cardiol.*, 2004, **43**, 474–482.
52 R. Raju, O. Vasconcelos, R. Granger and M. C. Dalakas, *J. Neuroimmunol.*, 2003, **141**, 125–131.
53 Y. Ge, R. J. Waldemer, R. Nalluri, P. D. Nuzzi and J. Chen, *PLoS One*, 2013, **8**, e68068.
54 Z. Chen, T. Laurentius, Y. Fait, A. Müller, E. Mückter, L. C. Bollheimer and M. Nourbakhsh, *J. Clin. Med.*, 2023, **12**, 3800.
55 F. Haugen, F. Norheim, H. Lian, A. J. Wensaas, S. Dueland, O. Berg, A. Funderud, B. S. Skålhegg, T. Raastad and C. A. Drevon, *Am J Physiol Cell Physiol*, 2010, **298**, C807–C816.
56 D. A. Kim, S. J. Park, J. Y. Lee, J. H. Kim, S. Lee, E. Lee, I.-Y. Jang, H.-W. Jung, J. H. Park and B.-J. Kim, *Endocrinol. Metab.*, 2021, **36**, 455–465.
57 J. B. Kurek, J. J. Bower, M. Romanella, F. Koentgen, M. Murphy and L. Austin, *Muscle Nerve*, 1997, **20**, 815–822.
58 W. Barnard, J. Bower, M. A. Brown, M. Murphy and L. Austin, *J. Neurol. Sci.*, 1994, **123**, 108–113.
59 S. A. Villeda, J. Luo, K. I. Mosher, B. Zou, M. Britschgi, G. Bieri, T. M. Stan, N. Fainberg, Z. Ding, A. Eggel, K. M. Lucin, E. Czirr, J. S. Park, S. Couillard-Després, L. Aigner, G. Li, E. R. Peskind, J. A. Kaye, J. F. Quinn, D. R. Galasko, X. S. Xie, T. A. Rando and T. Wyss-Coray, *Nature*, 2011, **477**, 90–94.
60 M. Ivanovska, Z. Abdi, M. Murdjeva, D. Macedo, A. Maes and M. Maes, *Pharmaceuticals*, 2020, **13**, 230.
61 K. A. Reardon, J. Davis, R. M. I. Kapsa, P. Choong and E. Byrne, *Muscle Nerve*, 2001, **24**, 893–899.
62 J. Grgic, L. C. McLlvenna, J. J. Fyfe, F. Sabol, D. J. Bishop, B. J. Schoenfeld and Z. Pedisic, *Sports Medicine*, 2019, **49**, 233–254.
63 T. P. Gavin, J. L. Drew, C. J. Kubik, W. E. Pofahl and R. C. Hickner, *Acta Physiol.*, 2007, **191**, 139–146.
64 J. P. Nederveen, S. Joanisse, C. M. L. Séguin, K. E. Bell, S. K. Baker, S. M. Phillips and G. Parise, *Acta Physiol.*, 2015, **215**, 177–190.
65 J. F. T. Fernandes, K. L. Lamb and C. Twist, *Sports*, 2019, **7**, 132.